Acetaminophen oxidation under solar light using Fe-BiOBr as a mild Photo-Fenton catalyst

Norma A. Ramos-Delgado [a,b,*], Diego A. Pino-Sandoval [c], Khirbet López-Velázquez [d], Christos Englezos [a], Minerva Villanueva-Rodríguez [c], Miguel A. Gracia-Pinilla [a,e,*], Nicolas D. Boscher [f], Han J.G.E. Gardeniers [a], Arturo Susarrey-Arce [a]

[a] *University of Twente, Mesoscale Chemical Systems, MESA+ Institute, P.O. Box 217, Enschede 7500AE, The Netherlands*
[b] *National Council of Science and Technology/National Technological Institute of Mexico - Campus Nuevo León. Center for Research and Technological Innovation, Apodaca, Nuevo León, Mexico*
[c] *Autonomous University of Nuevo Leon, Faculty of Chemistry Science, San Nicolás de los Garza, Nuevo León, Mexico*
[d] *Polytechnic University of Tapachula. Carretera Tapachula - Puerto Madero, Tapachula, Chiapas, Mexico*
[e] *Autonomous University of Nuevo Leon, Faculty of Physical and Mathematics Science. San Nicolás de los Garza, Nuevo León, Mexico*
[f] *Materials Research and Technology Department, Luxembourg Institute of Science and Technology, Esch-Sur-Alzette L-4362, Luxembourg*

ABSTRACT

Acetaminophen is an analgesic used as a first-choice treatment for pain and fever. When individuals consume acetaminophen, a portion of the drug is excreted through urine and can end up in wastewater. Water remediation from pharmaceuticals, such as acetaminophen, is required before reaching the environment. This work demonstrates that Fe–BiOBr using the solar photo-Fenton process eliminates acetaminophen at mild pH in aqueous media. Fe-BiOBr is produced using microwave-assisted solvothermal synthesis, and the formation of the BiOBr phase is confirmed with XRD. SEM and TEM demonstrated the flower-like morphology, in which crystallite size reduces as a function of the Fe loading. The chemical environment at the surface of Fe–BiOBr is investigated with XPS. The results are connected with Raman analysis, which suggests the presence of oxygen vacancies in Fe–BiOBr. Furthermore, the effect of Fe in BiOBr is assessed by determining the optical band gap with UV–Vis. The Fe-BiOBr functionality is assessed during acetaminophen degradation. Fe-BiOBr revealed excellent performance in degrading acetaminophen in the first minutes ($Q = 10$ kJ m^{-2}) under natural sunlight. Results reveal that 1% Fe content in BiOBr can degrade acetaminophen and its main byproduct (30 min, $Q = 50$ kJ m^{-2}) at pH 5 and using 0.25 gL^{-1} of catalyst. A synergistic mechanism between heterogeneous photocatalysis and Fenton processes with primary superoxide ($^{\bullet}O_2^-$) radical, followed by hydroxyl ($^{\bullet}OH$) radical and photogenerated holes (h^+), is proposed. Our research contributes to the degradation of pharmaceuticals under mild conditions and sunlight irradiation.

1. Introduction

Acetaminophen (ACP) is an analgesic used as a first-choice treatment for pain and fever [1]; an average of 4% can be excreted by humans through the urinary tract after intake [2], yielding high concentrations of ACP residues in wastewater [3]. The environmental impact of ACP is worrisome due to its high consumption during the COVID outbreak, which nearly tripled between 2019 and 2021 [4]. Some studies reported ACP concentrations in wastewater up to 22.8 μg/L in North Scotland, 51.22 μg/L in North Mexico, 105.8 μg/L in Singapore, and 667 μg/L in

Colombia [5–8]. In response to pharmaceutic discharges in wastewater, the European Union has implemented measures through the Water Framework Directive (WFD) to monitor and evaluate health risks associated with emerging contaminants. The Watch List (WL) is updated every two years to track the presence of contaminants and issue legal regulations, if necessary, to limit their environmental impact. Since 2020, the WL has included antibiotics like amoxicillin, ciprofloxacin, sulfamethoxazole, and trimethoprim, among others, to evaluate bacterial resistance. However, until now, ACP (Fig. 1) is not in the WL despite its high consumption and discharge [9], probably because it is not used
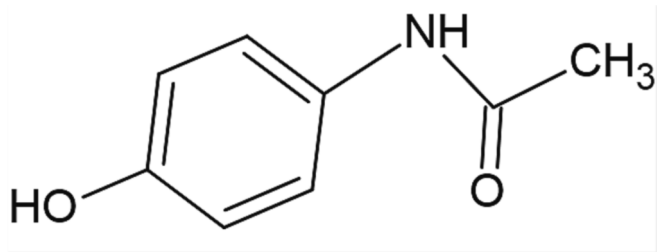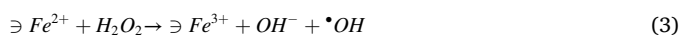
Fig. 1. ACP chemical structure.

as an antibiotic, although similar painkillers have been demonstrated to have antimicrobial properties [10,11], which might lead to creating resistance in microorganisms [12]. Like European countries, other countries like Mexico have not defined a permissible limit for the ACP in water. Other organizations, such as the Minnesota Department of Health (MDH) in the U.S.A., have established permitted levels of drinking water (200 μg/L) [13]. Similar guidelines, like in the U.S.A., should be followed since large concentrations of APC in water (4.46 μg/L) can lead to ecotoxicological risk in aquatic ecosystems, e.g., Daphnia magna has a half maximal effective concentration (EC_{50}) of 2.04 mg/L [14]. From this view, pharmaceuticals-free water is vital since it can lead to plant and animal genotoxic, mutagenic, and ecotoxicological effects [15].

Advanced oxidation processes (AOPs) can remove pharmaceuticals from water. The process involves the generation of radical species that oxidize organic molecules, such as ACP, until mineralization, i.e., the formation of innocuous products such as CO_2, H_2O, and inorganic salts. Among the AOPs, the photo-Fenton process produces hydroxyl radical $^{\bullet}OH$, a very reactive and highly oxidizing species. Homogeneous photo-Fenton uses iron salts to catalyze the decomposition of hydrogen peroxide to $^{\bullet}OH$. Nevertheless, it requires highly acidic conditions (pH 2–3) to avoid the formation of hydroxides, which leads to iron deactivation and limits photocatalytic activity. This is the case of photo-Fenton degradation of ACP, which has been studied to its finest detail [16–18]. Other photo-Fenton approaches require chelation and/or immobilization of iron (Fe) on solid surfaces, which are attractive options to overcome deactivation [19]. The approaches are known as heterogeneous Fenton or photo-Fenton if the light is involved in the degradation process [20]. The heterogeneous photo-Fenton degradation mechanism is a synergistic combination of photocatalysis like Fe and a semiconductor. When the light reaches the semiconductor, the photogenerated electrons in the conduction band are used to accelerate the Fenton redox reaction on the photocatalyst surface ($\ni Fe$) by increasing the cycle rate of Fe^{3+}/Fe^{2+}, which promotes the decomposition of H_2O_2, yielding strongly oxidizing $^{\bullet}OH$ [21]. For example, in Eq (1) to (6):

$$Catalyst + hv \rightarrow h^+ + e^- \tag{1}$$

$$\ni Fe^{3+} + e^- \rightarrow \ni Fe^{2+} \tag{2}$$

$$\ni Fe^{2+} + H_2O_2 \rightarrow \ni Fe^{3+} + OH^- + {}^{\bullet}OH \tag{3}$$

$$H_2O_2 + e^- \rightarrow {}^{\bullet}OH + OH^- \tag{4}$$

$$h^+ + OH^- \rightarrow {}^{\bullet}OH \tag{5}$$

$$H_2O + h^+ \rightarrow {}^{\bullet}OH + H^+ \tag{6}$$

Among the heterogeneous photo-Fenton catalysts to degrade ACP under controlled UV or visible light include Fe_3O_4, Fe_2O_3, Fe_2O_3-TiO_2-clay, $\alpha Fe_2O_3/g$-C_3N_4, F-$C_3N_4/NiFe_2O_4$ and zero-valent Fe [22–26]. Recently, BiOBr, a p-type semiconductor, has received attention because of its narrow band gap (2.62–2.90 eV) that allows degradation under visible light [27,28]. Photo-Fenton activity can increase further with the incorporation of Fe. Diverse approaches have been used to synthesize Fe-BiOBr, including solvothermal and microwave-assisted solvothermal.

A benefit of microwave-assisted solvothermal is that it is less time-consuming (~a few minutes to 1 h) [29–31] than conventional solvothermal (8 h) [32–34]. Time reduction can be related to uniform heating by electromagnetic waves and ease photocatalyst synthesis [34,35]. Applications of solvothermal synthesized Fe-BiOBr include the degradation of rhodamine B and bisphenol A [20], phenol [31], and atrazine [36], achieving complete degradation within 30 and 120 min. The main degradation mechanism has been suggested to be related to $^{\bullet}OH$ and h^+ as the main oxidizing species [31], of great similitude to the described chemical mechanism in Eq (1) to (6).

This work demonstrates that ACP can be degraded under solar illumination and mild conditions using low Fe loadings in Fe-BiOBr photo-Fenton catalyst synthesized using a less time-consuming microwave-assisted solvothermal method. The BiOBr phase in Fe-BiOBr is confirmed with XRD. SEM and TEM demonstrated the flower-like morphology, in which crystallite size reduces as a function of the Fe loading. The chemical environment at the surface of Fe–BiOBr is investigated with XPS. The results are connected with Raman analysis, which suggests the presence of oxygen vacancies in Fe–BiOBr. Furthermore, the effect of Fe in BiOBr is assessed by determining the optical band with UV–Vis. The Fe-BiOBr functionality is assessed during ACP photo-Fenton catalytic activity, carried out for 0.25 mg L^{-1} of catalyst load and pH 5. The latest conditions are most favorable since most international regulations allow wastewater discharges to surface water with a pH of 5.5 to 9.5 [37,38]. The Fe-BiOBr catalyst showed excellent performance in degrading ACP in less than 10 min ($Q = 10$ kJ m^{-2}) under natural sunlight. Our results can contribute to developing a Fenton photocatalyst to degrade pharmaceuticals under natural sunlight and mild conditions.

2. Experimental section

2.1. Materials

Bismuth nitrate pentahydrate ($Bi(NO_3)_3 \cdot 5H_2O$, 98%), hexadecyl trimethyl ammonium bromide (CTAB, 99%), ferric nitrate nonahydrate ($Fe(NO_3)_3 \cdot 9H_2O$, 99%) and ACP (>99%) were purchased from Sigma-Aldrich. Ethylene glycol (EG, 99%) was purchased from DEQ, Monterrey, Mexico. Methanol and HPLC water were purchased from Tedia Company.

2.2. Photocatalysts synthesis

The photocatalysts xFe-BiOBr (x = 1 and 3 wt% Fe) were synthesized as follows: 3 mmol of $Bi(NO_3)_3 \cdot 5H_2O$ and appropriate amounts of Fe $(NO_3)_3 \cdot 9H_2O$ (0.19 and 0.56 mmol) were dissolved in 30 mL of ethylene glycol by sonication; similarly, 3 mmol of CTAB were also dissolved in EG (30 mL). Subsequently, both clear dissolutions were mixed and stirred vigorously for 20 min and transferred to Teflon vessels of MARS 6 equipment (CEM Corp. USA) which was operated at 160 °C, 20 min, and 450 W. Later, the microwave vessels were cooled to room temperature, and solids were recuperated by centrifugation. The prepared materials were naturally cooled to room temperature, repeatedly washed with ethanol and distilled water, and dried in an oven at 80 °C for 12 h. As a reference, pristine BiOBr was prepared using the same procedure without the addition of Fe precursor.

2.3. Structural and morphological characterization

The photocatalysts xFe-BiOBr (x = 1 and 3 wt% Fe) morphology was analyzed using scanning electron microscopy (SEM, JEOL JSM6510-LV) equipped with an energy-dispersive X-ray detector (EDX) and high-resolution transmission electron microscope (HR-TEM), using FEI TITAN G2 80—300 (operated at 300 keV). X-ray diffraction (XRD) determined the catalysts' crystalline phase and crystallite size. XRD was carried out using a Bruker AXS Model D2 PHASER diffractometer (Cu Kα radiation, λ = 1.5406 Å) at a scan rate of 0.1°/s over a diffraction angle

2θ from 5 to 80°. The average crystallite sizes of the photocatalysts have been calculated according to the classical Scherrer's equation:

$$D = \frac{K\lambda}{\beta cos\theta_B} \tag{7}$$

where D is crystallite size (nm), K is a constant equal to 0.9, λ is X-ray wavelength (1.5406 Å), β is a half-high width of the diffraction peak (1 1 0), and θ_B is the 2θ diffraction angle [39].

2.4. Chemical composition and band gap determination

Chemical species in Fe-BiOBr were obtained using a Raman Thermo Scientific microscope with a laser diode as a radiation source (780 nm). Chemical species present at the surface of BiOBr and Fe-BiOBr were investigated with X-ray photoelectron spectroscopy (XPS). The spectra were recorded using a Thermofisher Nexsa G2 (Al-Kα, 1486.6 eV, 120 W). The amounts of Fe in the prepared photocatalysts were determined using atomic absorption spectroscopy (AAS, SpectrAA 220FS, Varian); before the AAS analysis, 0.015 g of each powder was digested in a mixture of HNO_3 and HCl (4:1) by microwave heating (MARS 6, CEM) for 20 min at 180 °C and 800 W. UV–Vis diffuse reflectance spectroscopy (UV–Vis/DRS) was recorded using a spectrophotometer Lambda 365 (Perkin Elmer) equipped with an integrating sphere using $BaSO_4$ as reference material. From the acquired spectra, the band gap (E_g) of the prepared catalysts was estimated by extrapolation from the plot of $[F(R) h\nu]^{1/n}$ vs. $h\nu$, where F(R) is the Kubelka-Munk function obtained from the UV–Vis diffuse reflectance data, $h\nu$ is the photon energy described by the Planck constant ($h = 4.135 \times 10^{-15}$ eV·s), and the light frequency (ν) given by the ratio of the speed of light (3×10^8 m/s) and the wavelength (m); n depends on transition characteristics of the semiconductor, a value of $n = 2$ was used due to BiOBr have indirect transitions [40].

2.5. Textural analysis

The specific surface area (SSA) of the catalysts was estimated by the Brunauer-Emmett-Teller method (BET), and pore sizes by the Barret-Joyner-Halenda method (BJH) using an N_2 adsorption–desorption equipment (TriStar II Plus, Micromeritics).

2.6. Photocatalytic activity

The experiments were carried out under natural sunlight in Apodaca City in Nuevo Leon, Mexico (25° 45′ N, 100° 7′ O). The photocatalytic activity of the catalysts was evaluated on the degradation of ACP solution (15 mgL⁻¹) (ACP, p-acetaminophen, $C_8H_9NO_2$) prepared using local drugs tablets (Medimart, 500 mg) in distilled water. The experiments were carried out in 100 mL of ACP solution on a Pyrex reactor, the pH was adjusted at 3 or 5 using HCl 0.1 M, and the catalyst added (0.25 gL⁻¹) was stirred for 30 min in darkness to allow the adsorption–desorption equilibrium between ACP and catalyst. After that, 102 μL of H_2O_2 (30% Fisherbrand, 10 mM) was added, and the reaction was conducted outdoors using natural sunlight. At regular intervals, samples were collected and filtered through a 0.45 μm nylon syringe filter to remove the photocatalyst. In solar degradation, once the light exposition started, the accumulated solar radiation was measured with a Delta OHM HD2102.2 radiometer (range: 315–400 nm), and samples were collected as needed, reaching a total of 300 kJ m⁻² for each experiment. ACP quantification was performed by liquid chromatography on HPLC Agilent Technologies 1260 Infinity equipment with diode array detector using a column Thermo Scientific Accucore C18 (150 × 4.6 mm). The mobile phase was a mixture of 25:75 v/v methanol (HPLC grade, Tedia) and 4% (v/v) acetic acid prepared in water, and the flow rate was 1.5 mL min⁻¹. The injection volume was 25 μL, and the detection wavelength (λ) was 242 nm. Similar tests were carried out under simulated solar radiation until reaching an accumulated energy of 300 kJ m⁻²

(Solar simulator Suntest, XLS + Model Atlas, Germany, equipped with a daylight filter that emits radiation from 300 to 800 nm). The mineralization degree was determined by the total organic carbon (TOC) diminished on a Shimadzu TOC-V CSH analyzer with an ASI-V model autosampler. Finally, to determine the main reactive species involved in ACP degradation, different scavengers of radicals were added in degradation tests under the same studied conditions. For this, *ter*-butanol (TBA, 5 mM), *p*-benzoquinone (BQ, 0.5 mM), and sodium oxalate (OXA, 5 mM) were added as •OH, •O_2^- and h^+ quenchers. All experiments were carried out in duplicates. The experiments have been carried out in duplicates. The difference between each pair of experiments was less than 10%; in the end, all reached total ACP degradation.

3. Results and discussions

A BiOBr photocatalyst with Fe is synthesized via the microwave-assisted solvothermal method. The synergy between Fe and BiOBr is investigated morphologically, structurally, chemically, and optically. Fe-BiOBr functionality is assessed during the photocatalytic degradation of ACP under solar irradiation. Finally, a photocatalytic action mechanism is proposed.

3.1. Morphological and structural characteristics of Fe-BiOBr

The morphology of the synthesized BiOBr and BiOBr loaded with 1 wt% (1Fe-BiOBr) and 3 wt% (3Fe-BiOBr) of Fe is investigated with SEM, as shown in Fig. 2. In Fig. 2 (a), BiOBr has spherical flower-like morphology, which is assembled by nanosheets in the form of interlocking petals, with interstitial spaces between them [32]. No apparent morphological differences exist between BiOBr and 1Fe-BiOBr and 3Fe-BiOBr in Fig. 2 (b) and 2 (c), showing the same morphology and behavior as BiOBr and Fe-BiOBr materials reported by others [31,41,42]. Fig. 2 (d) shows an SEM- EDX map of the 1Fe-BiOBr image to compare with (d1) Bi, (d2) Br, and (d3) Fe elemental composition. This analysis reveals that the elements present in the samples are homogeneously distributed, confirming that the microwave-assisted solvothermal synthesis method is suitable for this material.

The morphological and structural properties are further investigated with TEM. Fig. 3 shows TEM, STEM-HAADF, and HR-TEM images for (a, b, c) BiOBr, (d, e, f) 1Fe-BiOBr, and (g, h, i) 3Fe-BiOBr. TEM images (a, d, and g) reveal that the structure retained a flower-like shape with a size of approximately 1.5 μm and did not show morphological changes as the Fe content increased. However, it seems that the 3Fe-BiOBr is less dense than BiOBr and 1Fe-BiOBr. STEM-HAADF images (b, e, and h) confirm the intercalated sheet-like morphology characteristics of BiOBr. Nevertheless, 3Fe-BiOBr has a bright core and darker spike-like features in a different sample area; bright dark regions can be associated with regions with heavier atoms, most probably from Bi. HR-TEM images (c, f, and i) show the presence of crystals with sizes around 10 nm. The crystal size decreases with increasing iron content, which is consistent with the XRD results in Fig. 4a. In Fig. 3, high crystallinity and lattice fringes with an interplanar lattice spacing of 0.36, 0.23 and 0.27 nm are estimated and assigned to BiOBr (1 0 1), (1 1 2), and (1 1 0) crystallographic planes. 1Fe-BiOBr and 3Fe-BiOBr exhibit slightly smaller crystallites compared to BiOBr.

The XRD diffraction pattern, displayed on Fig. 4a, for BiOBr matches with the tetragonal phase (JCPDS 00–001-1004), in which the prominent peaks at angles 11.0°, 25.1°, 31.9°, 32.3°, 39.4°, 46.3°, and 57.2° are assigned to (0 0 1), (1 0 1), (1 0 2), (1 1 0), (1 1 2), (2 0 0) and (2 1 2) planes [43,44]. The XRD patterns for 1Fe-BiOBr and 3Fe-BiOBr show similar diffraction peaks but broadened. This can be related to the presence of Fe, which decreases the diffraction peaks' relative intensity, indicating that Fe ions hinder grain growth [32]. These results are consistent with TEM observations in Fig. 3. Small crystallites will tend to increase the specific surface area as Fe content increases [32,45]. This has been confirmed with BET and discussed in detail in Supporting
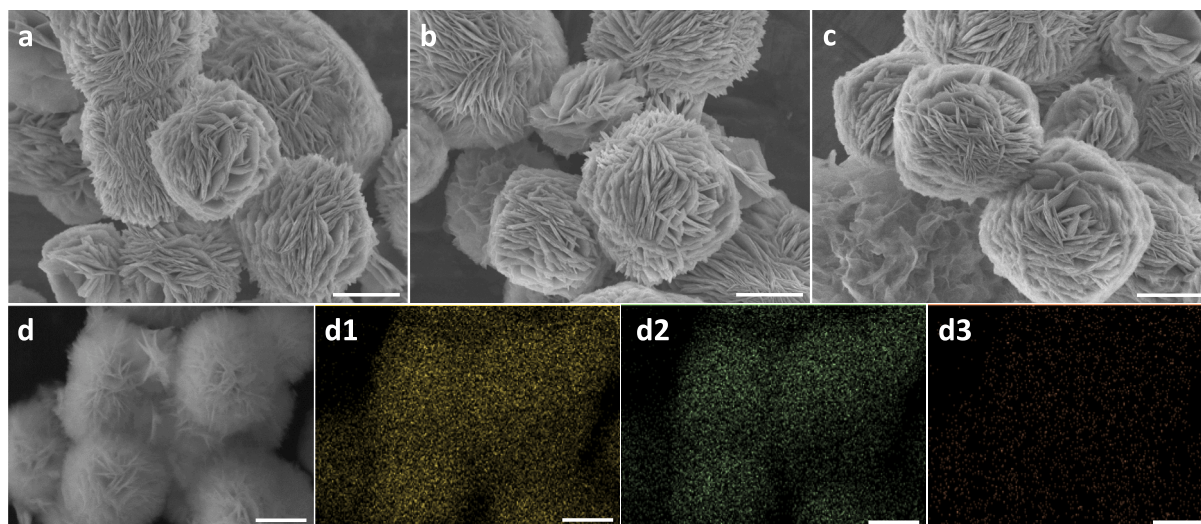
Fig. 2. SEM images of a) BiOBr, b) 1Fe-BiOBr, c) 3Fe-BiOBr, d) SEM image of 1Fe-BiOBr, followed by the EDX mapping for d1) Bi, d2) Br, d3) Fe. The scale bar represents 1 μm.
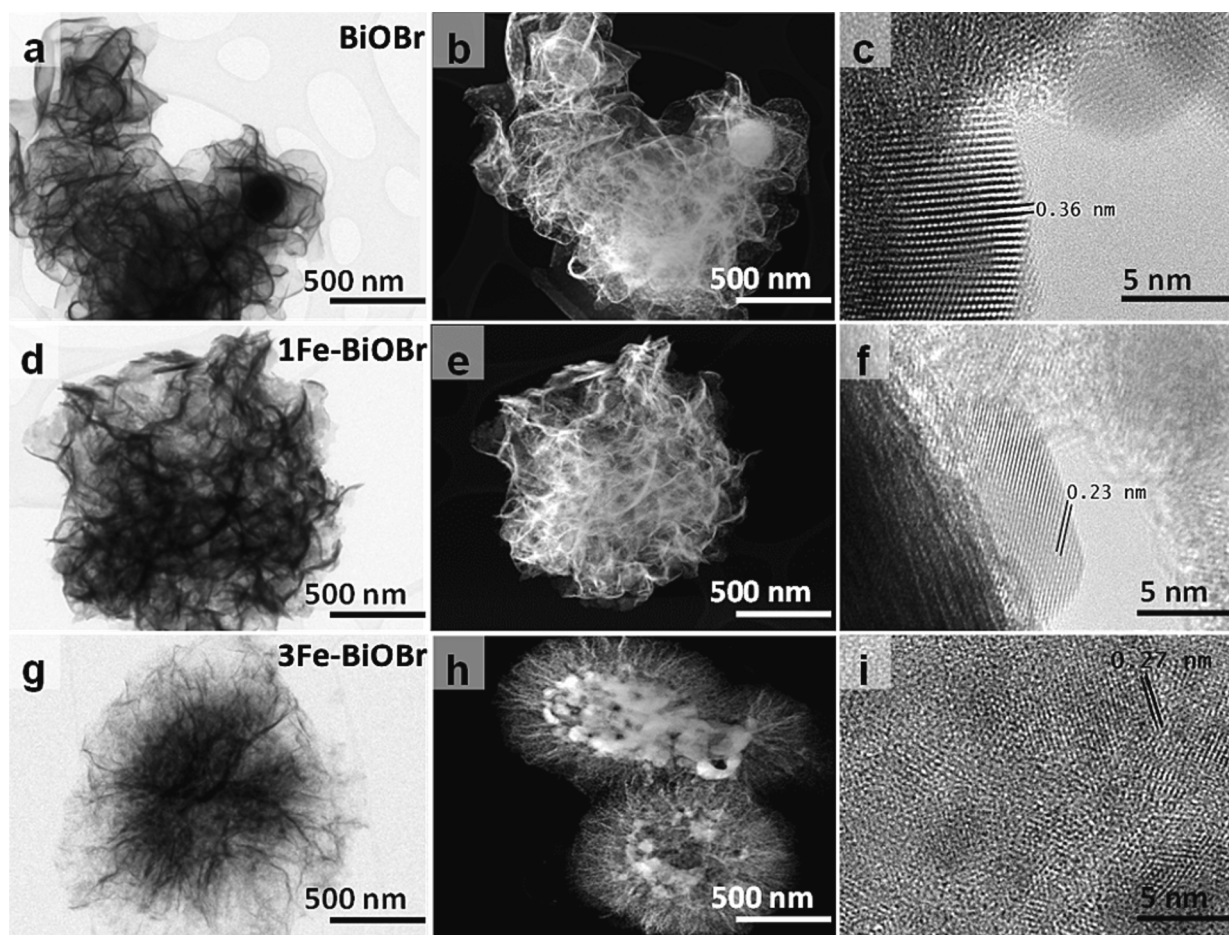

Fig. 3. TEM images for (a, b, c) BiOBr, (d, e, f) 1Fe-BiOBr, and (g, h, i) 3Fe-BiOBr. TEM, STEM-HAADF, and HR-TEM (in the first, second, and third columns, respectively).

Information, see **Fig. S1**. The results are presented in Table 1. The crystal size of the photocatalysts is calculated, and BiOBr, 1Fe-BiOBr, and BiOBr, 3Fe-BiOBr have crystallite size of 12.9, 7.8, and 6.4 nm.

The optical properties of BiOBr, 1Fe-BiOBr, and 3Fe-BiOBr are measured using UV–Vis DRS in Fig. 4**b** to estimate and compare the bandgap. BiOBr has a steep increase of absorption at wavelengths shorter than 413 nm, which can be assigned to the intrinsic band gap of pure BiOBr (~3.00 eV) [45]. The spectra of 1Fe-BiOBr, and 3Fe-BiOBr exhibit a redshift and increased photoabsorption in the visible light range and near-infrared region [31,32], which can indicate the Fe
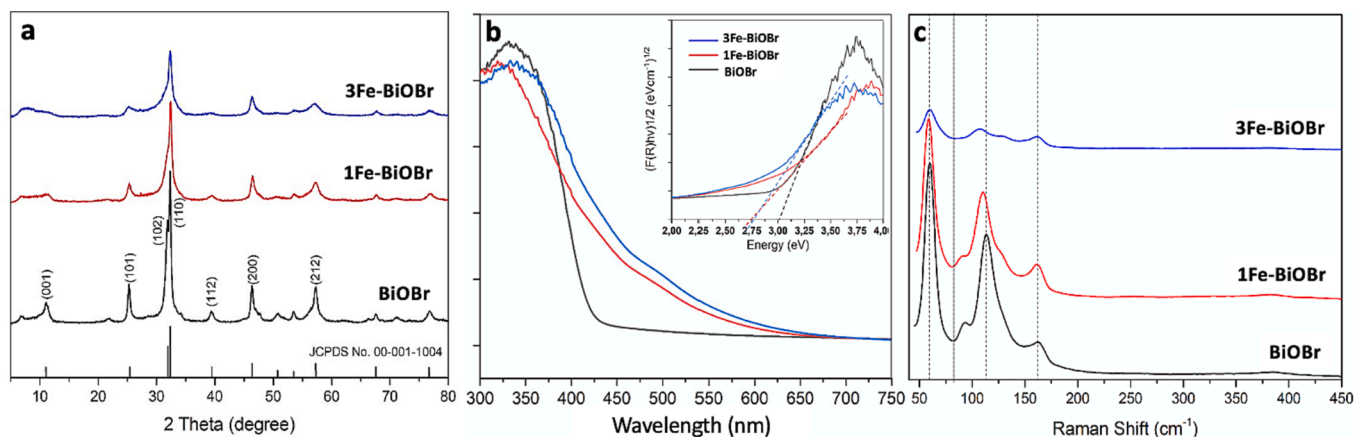
Fig. 4. Structural and optical properties of BiOBr (black line), 1Fe-BiOBr (magenta line), and 3Fe-BiOBr (blue line), (a) XRD patterns, (b) UV–Vis DRS spectra and (c) Raman spectra.

Table 1
Displays the estimated band gap, crystallite size, specific surface area, and Fe content in BiOBr, 1Fe-BiOBr, and 3Fe-BiOBr.

| Catalyst	E_g (eV)	Crystallite size (nm)	Specific surface area (m^2/g)	Incorporated Fe (wt%)	
				[a]EDX	[b]AAS
BiOBr	3.00	12.9	7.09	–	–
1Fe-BiOBr	2.73	7.8	16.26	1.0	0.96
3Fe-BiOBr	2.75	6.7	21.86	3.01	2.78

loading. This observation is also reflected in the color change of these materials from white to reddish yellow. A possible mechanism for such redshift may be related to the transition of electrons between the conduction band or valence band of BiOBr and Fe ions or the internal transfer charge between Fe ions ($Fe^{3+} + Fe^{3+} \rightarrow Fe^{4+} + Fe^{2+}$) [32,46,47]. The band gap (E_g) for 1Fe-BiOBr and 3Fe-BiOBr are in the order of 2.73 and 2.75 eV (Table 1).

Raman analysis in Fig. 4c shows the characteristic bands of BiOBr observed at 56.8, 95.0, 112.4, and 163.0 cm^{-1} [48], which are assigned to the internal Bi-Br stretching modes [49]. Likewise, a weak and broad signal corresponding to the motion of oxygen atoms is observed at 385 cm^{-1} [50], and the signal at 86 cm^{-1} is ascribed to the formation of oxygen vacancies (OVs) [51]. It should be noted that the Raman signal

for BiOBr is the most intense, indicating its higher crystallinity than the 1Fe-BiOBr and 3Fe-BiOBr. Furthermore, the decrease in the intensity of the Raman signal is attributed to the formation of oxygen vacancies [52]. These results are coherent with TEM (Fig. 3) and XRD (Fig. 4a) analyses. Compared to BiOBr, a blue shift for 1Fe-BiOBr and 3Fe-BiOBr is observed. These variations could be associated with changes in the structural and chemical environment in BiOBr due to the incorporation of Fe.

3.2. Chemical species at the surface of Fe-BiOBr

XPS analysis confirmed the elemental compositions of BiOBr, 1Fe-BiOBr, and 3Fe-BiOBr. The XPS spectra are shown in Fig. 5; the signals present in samples are Br 3d (**a**), Bi 4f (**b**), O 1 s (**c**), and Fe 2p (**d**). The high-resolution XPS Fe 2p core level spectra illustrate the increasing iron concentration in BiOBr, 1Fe-BiOBr, and 3Fe-BiOBr (Fig. 5d). The Fe 2p3/2 and Fe 2p1/2 contributions located at ca. 711.5 eV and ca. 725.1 eV suggest the insertion of Fe^{3+} in BiOBr [31,53,54]. The presence of Fe in 1Fe-BiOBr before and after the reaction is shown in **Fig. S2**; no major differences in Bi, O, Br, and Fe content have been found. However, in **Table S1**, a slight reduction in the Fe content in the used catalyst is observed, which can be explained by an increase in the carbon content due to the pollutant adsorption or a low iron leaching [55,56]. For all studied samples, the high-resolution XPS spectra of the Br 3d (Fig. 5a)
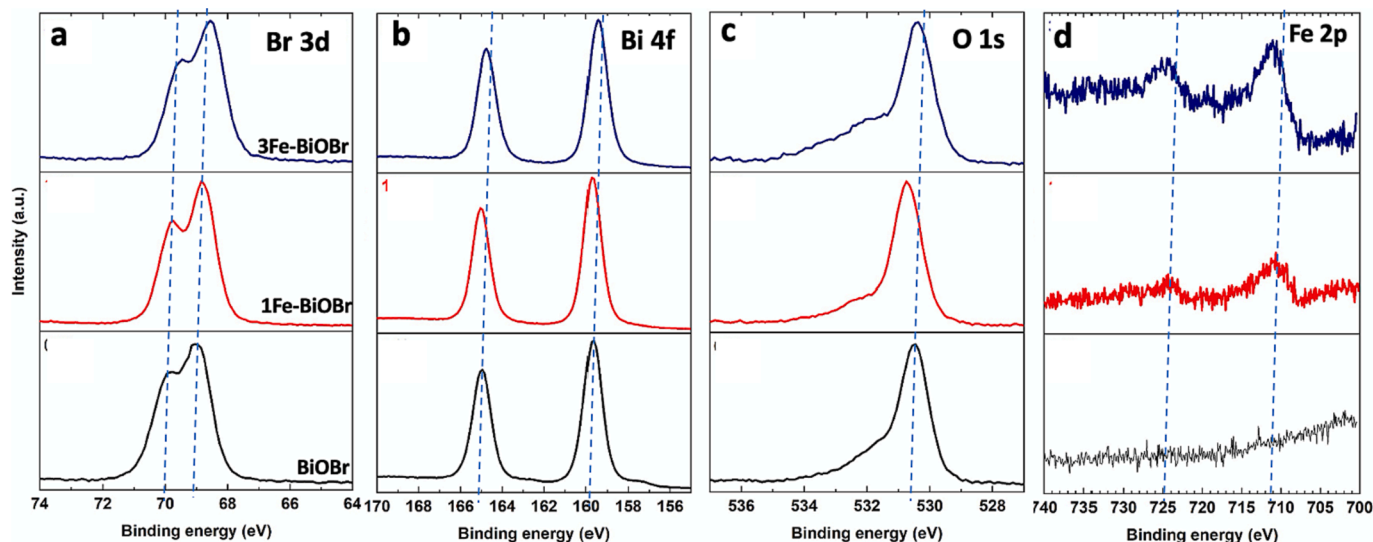
Fig. 5. XPS spectra (Br 3d, Bi 4f, O 1 s and Fe 2p) of pure BiOBr, 1Fe-BiOBr, and 3Fe-BiOBr.

and Bi 4f core levels (Fig. 5b) revealed the contribution of doublet pairs, i.e., Br 3d5/2 at ca. 68.7 eV and Br 3d3/2 at ca. 69.7 eV and Bi 4f7/2 at ca. 159.4 eV and Bi 4f5/2 at ca. 164.8 eV (indicating the presence of Bi^{3+} in the materials) [57,58]. The high-resolution XPS O 1 s core level spectra all exhibit a dominant contribution at ca. 530.5 eV attributed to O in BiOBr (Fig. 5c). Additional contributions, ascribed to surface-adsorbed oxygen, H_2O, and –OH groups [54,57,59], are also detected at higher binding energies (ca. 532.0–534.0 eV).

3.3. Photocatalytic activity of Fe-BiOBr

The solar photo-Fenton is conducted under natural sunlight to oxidate ACP using Fe-BiOBr is showcased. Fig. 6 shows the degradation of ACP [mg/L] as a function of the solar accumulated energy Q [kJ/m^2]. For 1Fe-BiOBr and 3Fe-BiOBr in Fig. 6a and 6b, ACP is degraded in the first minutes ($Q = 10$ kJ m^{-2}) (closed circles and squares). Concurrently, the ACP byproduct is formed (open circles and squares) and progressively degraded. For BiOBr, ACP degradation is not achieved until 240 kJ/m^2 (i.e., 2.5 h) in Fig. S3. Fig. 6a and 6b show that 15 mg/L of ACP and its main byproduct is fully degraded in 30 min under natural solar light and 10 mM of H_2O_2. It is important to highlight that under solar irradiation, 1Fe-BiOBr and 3Fe-BiOBr degrade ACP at mild pH conditions, i.e., close to pH 5. At pH 5, more byproduct (Bypr) is produced (Fig. 6a and 6b), similar to the obtained by homogeneous solar photo-Fenton, where hydroxylated species are initially formed as intermediates, improving the degradation of ACP. Such species can lead to an improvement in the reduction of Fe^{3+} to Fe^{2+} in comparison to more recalcitrant intermediates produced, such as acetamide, hydroquinone, or benzoquinone (Fig. S4) [17,60]. Regarding the mineralization percentage, this has been measured using TOC (Fig. 6c). The 1Fe-BiOBr achieved the highest mineralization of ACP ca. 58% at pH 5, similar to what was reported for atrazine and bisphenol A, under visible light, but at pH 3 using similar catalysts [31,36]. The results represent a great advantage of our system under natural solar light and pH 5, considered mild conditions.

The results demonstrate that 1Fe-BiOBr promotes the degradation of ACP. Since the estimated Eg are similar (Fig. 4b), variation in the product degradation can be related to the higher degree of crystallinity of 1Fe-BiOBr shown in Fig. 3f and Fig. 4a. Higher degree of crystallinity of 1Fe-BiOBr can promote the necessary pathway to charge carriers to be readily available, possibly degrading ACP side-products more efficiently [61]. Moreover, the effect of OVs in 1Fe-BiOBr should not be disregarded.

We further essay APC degradation under controlled solar irradiance (i.e., solar simulator), using 1Fe-BiOBr at pH 3 and pH 5. The results compare with ACP photo-oxidation without H_2O_2 (photocatalysis) and with H_2O_2 (photo-Fenton) in Fig. 7. The photocatalytic degradation of ACP shows a significantly better performance in the presence of H_2O_2

(Fig. 7a). At pH 5 ACP oxidation without H_2O_2 is slightly better; the results are in accordance with other studies and relate to the surface interaction between ACP and the catalyst [62]. The results of the heterogeneous photo-Fenton process (with H_2O_2) show that the pH has a low effect since similar outcomes are obtained at pH 3 and 5 (Fig. 7a). Nevertheless, pH 5 is attractive for the process because it is well-known that the limitation of the Fenton reaction often needs more acidic conditions (near pH 3) to achieve maximum performance and avoid iron precipitation at higher values. On the other hand, iron leaching in an acidic medium has been widely reported and depends on the catalyst's stability. However, it has been observed that low iron leaching and the presence of chelating agents (such as organic acids or byproducts) could contribute to contaminant elimination through the homogeneous Fenton reaction [55,56]. This phenomenon could explain the slight degradation increase at pH 3 in Fig. 7c compared to these observed at pH 5.

The effectiveness of natural solar illumination is contrasted with controlled solar irradiance. Compared with solar irradiation (Fig. 6), results in Fig. 7a show longer times for ACP degradation, close to 2 h ($Q = 150$ kJ m^{-2}). Furthermore, for the byproducts, a longer time is needed for degradation, ca. 4 h (Fig. 7b). The main difference between the photocatalytic experiments under solar light and controlled solar irradiance is the solar energy contribution, thus affecting the degradation times. In other words, the solar spectrum has UV, Vis, and IR contributions, while controlled solar irradiance might not fully include UV contributions (Fig. S5). The results explain the benefit of natural solar light-induced reactions, which use a significant portion of the solar spectrum.

It is well known that heterogeneous photo-Fenton results from a synergistic combination of photocatalysis and Fenton reaction processes. Therefore, it is important to compare the mineralization with and without H_2O_2 (Fig. 7c). Here, higher mineralization is observed in heterogeneous photo-Fenton than in photocatalysis. In the latest, the •OH is mainly produced by splitting water in the valence band, while in heterogeneous photo-Fenton, the possibility of producing –OH is greatly increased, and other oxidizing species may also play an important role. To clarify the main species involved in ACP degradation by the synergistic combination of photocatalytic and Fenton processes using 1Fe-BiOBr, p-benzoquinone (BQ), sodium oxalate (OXA), and tert-butanol (TBA) are used as radical scavengers of superoxide radicals (•O_2^-), h^+ and •OH, respectively [30]. As seen in Fig. 8, total ACP degradation is achieved using 1Fe-BiOBr + H_2O_2 without adding any quencher. In contrast, when TBA and OXA are added during degradation, diminishes 20% and 30% of ACP, which proved that •OH and h^+ play a significant role in the heterogeneous photo-Fenton process. However, the ACP degradation dropped abruptly (60 %) in the presence of BQ, indicating that •O_2^- is the most important active species in the synergistic degradation process. The results demonstrate that •O_2^-, followed by $h^{+,}$ and •OH contribute to the degradation of ACP, prominently produced under
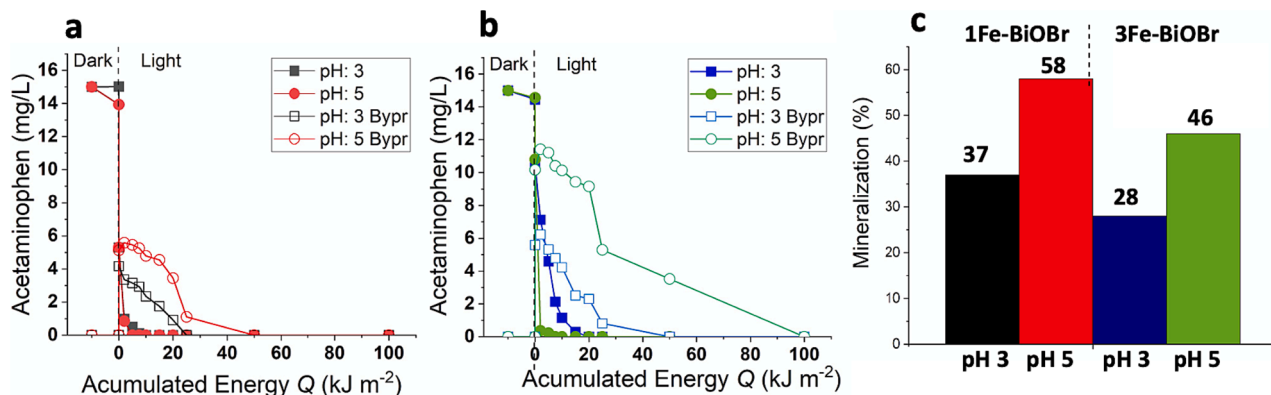

Fig. 6. ACP degradation by heterogeneous solar photo-Fenton using (a) 1Fe-BiOBr and (b) 3Fe-BiOBr and (c) TOC reduction as mineralization percentage ($C_{0\ ACP}$ = 15 mg/L, Catalyst load = 0.25 g/L, H_2O_2 = 10 mM). The experiments have been carried out in duplicates.
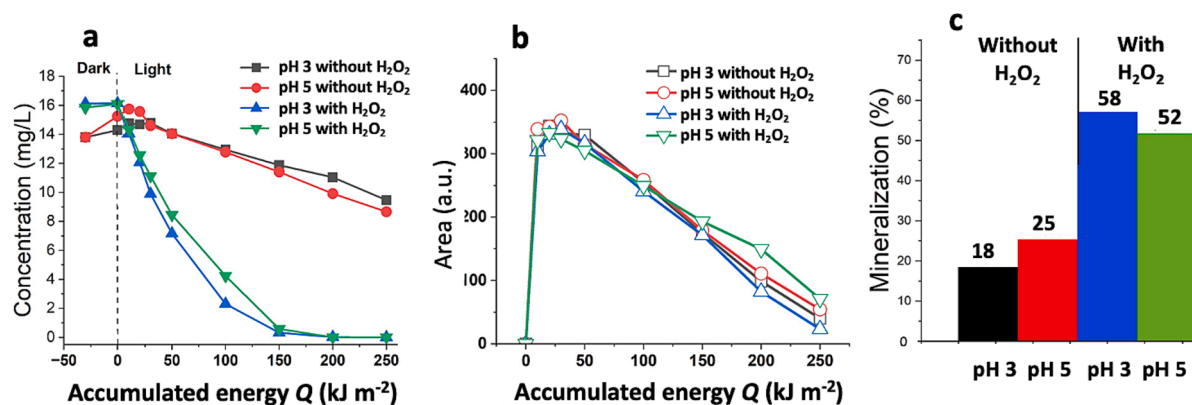
Fig. 7. (a) ACP degradation, (b) Byproduct generation, and (c) TOC expressed as mineralization percentage using 1Fe-BiOBr (without H_2O_2) and photo-Fenton (with H_2O_2) under simulated solar light. ($C_{0\ ACP}$ = 15 mg/L, Catalyst load = 0.25 g/L, H_2O_2 = 10 mM). The experiments have been carried out in duplicates.
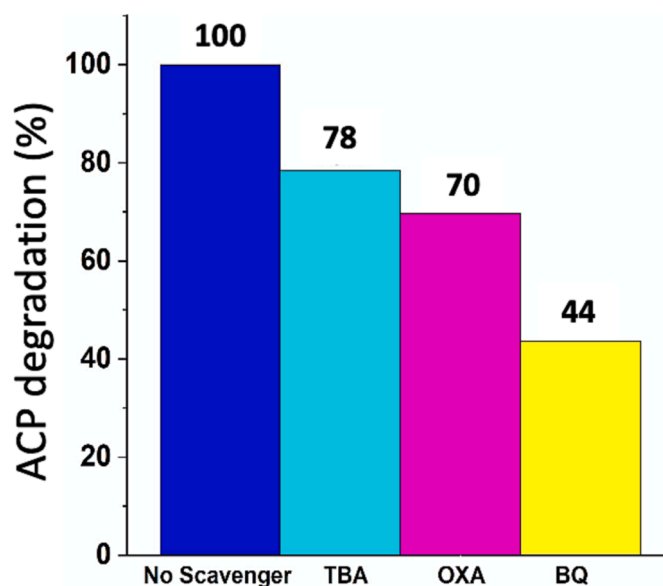

Fig. 8. ACP degradation with scavengers using 1Fe–BiOBr. ($C_{0\ ACP}$ = 15 mg/L, Catalyst load = 0.25 g/L, H_2O_2 = 10 mM, pH = 5).

natural solar light irradiation.

3.4. Proposed mechanism for the photo–Fenton system

From our results, the proposed reaction mechanism for ACP degradation by heterogeneous photo–Fenton using Fe–BiOBr considers the synergy between photocatalysis and Fenton processes. The mechanism from Fig. 9 considers solar irradiation, which promotes photoelectrons (e^-) generation at the CB and holes (h^+) at the VB; the e^- is moved to the surface of BiOBr and is used to reduce Fe^{3+} (Fe(III)) to Fe^{2+} (Fe(II)). This leads the Fe(III)/Fe(II) cycle over the BiOBr surface and promotes the active generation of $^\bullet OH$ in the presence of H_2O_2. Within this cycle, Fe (II) can react with oxygen O_2 in the presence of protons (H^+) to generate Fe (III), which can then be reduced and participate in further cycles of the photo-Fenton reaction. In addition, the e^- available in the OVs can react with the H_2O_2 to form $^\bullet OH$. On the other hand, the h^+ in the VB contributes to the $^\bullet OH$ generation by splitting the H_2O molecule. Also, h^+ can degrade ACP by direct oxidation. It is worth highlighting the importance of OVs in the process. OVs involve releasing two electrons per removed oxygen on the surface [63] that can act as an electron pump, leading to the formation of $^\bullet O_2^-$ radicals. It is proposed that $^\bullet O_2^-$ is the most important oxidant species for this system, in which the
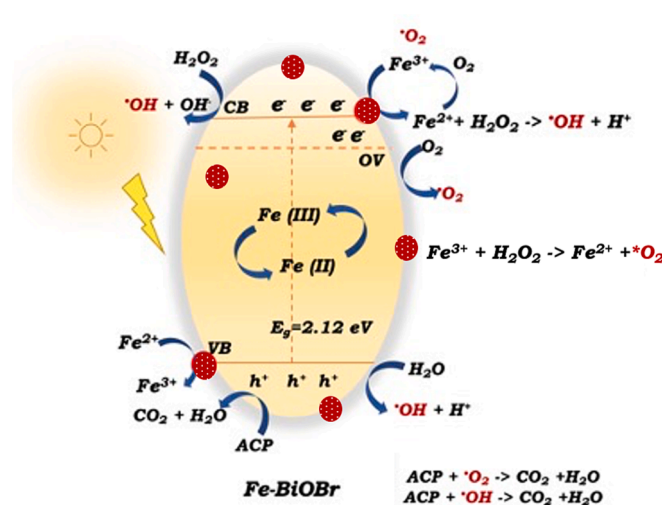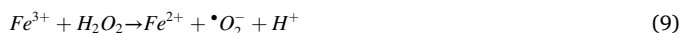

Fig. 9. Proposed reactions mechanism by heterogeneous photo-Fenton for ACP degradation under solar light.

generation takes place in three ways: i) traditionally, the dissolved oxygen reacts with e^- photogenerated or those in the OV to form $^\bullet O_2^-$ (8), ii) H_2O_2 can reduce Fe^{3+} to Fe^{2+} and produce $^\bullet O_2^-$ and H^+ (9) and iii) adsorbed O_2 can oxidize Fe^{2+} to produce Fe^{3+} and $^\bullet O_2^-$ radical (10).

$$O_{2(disol)} + e^- \rightarrow {}^\bullet O_2^- \tag{8}$$

$$Fe^{3+} + H_2O_2 \rightarrow Fe^{2+} + {}^\bullet O_2^- + H^+ \tag{9}$$

$$Fe^{2+} + O_{2(ads)} \rightarrow Fe^{3+} + {}^\bullet O_2^- \tag{10}$$

These mechanisms inhibit the recombination of photogenerated h^+/e^- pairs and favor the Fenton degradation process. The proposed mechanism can explain the observed effect for 1Fe-BiOBr, which shows a higher ACP degradation.

3.5. Conclusions

Fe–BiOBr has been successfully synthesized by microwave-assisted solvothermal method and exhibited excellent degradation activity in the solar photo-Fenton system, which allowed the total and almost immediate ACP removal at mild conditions. The results highlight that 1% Fe content in BiOBr is enough to degrade ACP and its main byproduct (30 min, Q = 50 kJ m^{-2}) at pH 5 and using 0.25 gL^{-1} of catalyst loading. The incorporated Fe in the BiOBr with a spherical flower-like shape decreased the recombination of photocarriers e^-/h^+ and favored the

generation of OVs. The solar photo–Fenton yield for ACP degradation is attributed to the synergistic combination of heterogeneous photo-catalysis and Fenton reaction processes. This leads the Fe(III)/Fe(II) cycle over the surface catalyst in the presence of light and H_2O_2. The main active species involved in this process were confirmed to be superoxide radicals ($^\bullet O_2^-$), followed by photogenerated holes (h^+) and hydroxyl radicals ($^\bullet OH$). Our research reliably contributes to the development of Fenton photocatalysts for degrading pharmaceuticals under mild conditions and natural sunlight irradiation.

Funding

CRediT authorship contribution statement

Norma A. Ramos-Delgado: Writing – original draft, Supervision, Resources, Conceptualization. **Diego A. Pino-Sandoval:** Validation, Investigation. **Khirbet López-Velázquez:** Methodology, Investigation, Formal analysis. **Christos Englezos:** Validation, Investigation. **Minerva Villanueva-Rodríguez:** Validation, Resources, Methodology. **Miguel A. Gracia-Pinilla:** Writing – original draft, Resources, Investigation, Formal analysis. **Nicolas D. Boscher:** Resources, Formal analysis. **Han J.G.E. Gardeniers:** Project administration, Funding acquisition. **Arturo Susarrey-Arce:** Writing – review & editing, Visualization, Resources, Project administration.

Declaration of Competing Interest

The authors declare that they have no known competing financial interests or personal relationships that could have appeared to influence the work reported in this paper.

Data availability

Data will be made available on request.

Acknowledgements

Appendix A. Supplementary data

Supplementary data to this article can be found online at https://doi.org/10.1016/j.jphotochem.2023.115124.

References

[1] V. Reinstadler, V. Ausweger, A.L. Grabher, M. Kreidl, S. Huber, J. Grander, S. Haslacher, K. Singer, M. Schlapp-Hackl, M. Sorg, H. Erber, H. Oberacher, Monitoring drug consumption in Innsbruck during coronavirus disease 2019 (COVID-19) lockdown by wastewater analysis, Sci. Total Environ. 757 (2021), 144006, https://doi.org/10.1016/j.scitotenv.2020.144006.

[2] J.A.H. Forrest, J.A. Clements, L.F. Prescott, Clinical Pharmacokinetics of Paracetamol, Clin. Pharmacokinet. 7 (1982) 93–107, https://doi.org/10.2165/00003088-198207020-00001.

[3] J.A. Yáñez, S.A. Chung, B.R. Román, P.J. Hernández-Yépez, F.O. Garcia-Solorzano, S. Del-Aguila-Arcentales, F. Inga-Berrospi, C.R. Mejia, A. Alvarez-Risco, Prescription, over-the-counter (OTC), in: Herbal, and Other Treatments and Preventive Uses for COVID-19, 2021, https://doi.org/10.1016/B978-0-323-85780-2.00001-9.

[4] A. Galani, N. Alygizakis, R. Aalizadeh, E. Kastritis, M.A. Dimopoulos, N. S. Thomaidis, Patterns of pharmaceuticals use during the first wave of COVID-19 pandemic in Athens, Greece as revealed by wastewater-based epidemiology, Sci. Total Environ. 798 (2021), 149014, https://doi.org/10.1016/j.scitotenv.2021.149014.

[5] C. Nebot, R. Falcon, K.G. Boyd, S.W. Gibb, Introduction of human pharmaceuticals from wastewater treatment plants into the aquatic environment: a rural perspective, Environ. Sci. Pollut. Res. 22 (2015) 10559–10568, https://doi.org/10.1007/s11356-015-4234-z.

[6] R. Hernández-Tenorio, J.L. Guzmán-Mar, L. Hinojosa-Reyes, N. Ramos-Delgado, A. Hernández-Ramírez, Determination of pharmaceuticals discharged in wastewater from a public hospital using lc-ms/ms technique, J. Mex. Chem. Soc. 65 (2021) 94–108, https://doi.org/10.29356/jmcs.v65i1.1439.

[7] N.H. Tran, K.Y.H. Gin, Occurrence and removal of pharmaceuticals, hormones, personal care products, and endocrine disrupters in a full-scale water reclamation plant, Sci. Total Environ. 599–600 (2017) 1503–1516, https://doi.org/10.1016/j.scitotenv.2017.05.097.

[8] E.A. Serna-Galvis, A.M. Botero-Coy, M. Rosero-Moreano, J. Lee, F. Hernández, R. A. Torres-Palma, An Initial Approach to the Presence of Pharmaceuticals in Wastewater from Hospitals in Colombia and Their Environmental Risk, Water (Switzerland). 14 (2022) 1–14, https://doi.org/10.3390/w14060950.

[9] O.F.S. Khasawneh, P. Palaniandy, Occurrence and removal of pharmaceuticals in wastewater treatment plants, Process Saf. Environ. Prot. 150 (2021) 532–556, https://doi.org/10.1016/j.psep.2021.04.045.

[10] A. Uneputty, A. Dávila-Lezama, D. Garibo, A. Oknianska, N. Bogdanchikova, J. F. Hernández-Sánchez, A. Susarrey-Arce, Strategies applied to modify structured and smooth surfaces: A step closer to reduce bacterial adhesion and biofilm formation, Colloid Interface Sci. Commun. 46 (2022), 100560, https://doi.org/10.1016/J.COLCOM.2021.100560.

[11] I. Sorzabal-Bellido, Y.A. Diaz-Fernandez, A. Susarrey-Arce, A.A. Skelton, F. McBride, A.J. Beckett, I.A. Prior, R. Raval, Exploiting Covalent, H-Bonding, and π-πInteractions to Design Antibacterial PDMS Interfaces That Load and Release Salicylic Acid, ACS Appl. Bio Mater. 2 (2019) 4801–4811, https://doi.org/10.1021/acsabm.9b00562.

[12] Y. Jia, Z. Wang, D. Fang, B. Yang, R. Li, Y. Liu, Acetaminophen promotes horizontal transfer of plasmid-borne multiple antibiotic resistance genes, Sci. Total Environ. 782 (2021), 146916, https://doi.org/10.1016/J.SCITOTENV.2021.146916.

[13] Minnesota Department of Health, Comparison of state water guidance and federal drinking water standards, (2021). https://doi.org/https://www.health.state.mn.us/communities/environment/risk/guidance/waterguidance.html.

[14] J.A. Rivera-Jaimes, C. Postigo, R.M. Melgoza-Alemán, J. Aceña, D. Barceló, M. López de Alda, Study of pharmaceuticals in surface and wastewater from Cuernavaca, Morelos, Mexico: occurrence and environmental risk assessment, Sci. Total Environ. 613–614 (2018) 1263–1274, https://doi.org/10.1016/j.scitotenv.2017.09.134.

[15] K. Samal, S. Mahapatra, M. Hibzur Ali, Pharmaceutical wastewater as Emerging Contaminants (EC): treatment technologies, impact on environment and human health, Energy Nexus. 6 (2022), 100076, https://doi.org/10.1016/j.nexus.2022.100076.

[16] M.G. Alalm, A. Tawfik, S. Ookawara, Degradation of four pharmaceuticals by solar photo-Fenton process: kinetics and costs estimation, J. Environ. Chem. Eng. 3 (2015) 46–51, https://doi.org/10.1016/j.jece.2014.12.009.

[17] A.G. Trovó, R.F. Pupo Nogueira, A. Agüera, A.R. Fernandez-Alba, S. Malato, Paracetamol degradation intermediates and toxicity during photo-Fenton treatment using different iron species, Water Res. 46 (2012) 5374–5380, https://doi.org/10.1016/j.watres.2012.07.015.

[18] A. Durán, J.M. Monteagudo, A. Carnicer, M. Ruiz-Murillo, Photo-Fenton mineralization of synthetic municipal wastewater effluent containing acetaminophen in a pilot plant, Desalination 270 (2011) 124–129, https://doi.org/10.1016/j.desal.2010.11.032.

[19] I. Oller, S. Malato, Photo-Fenton applied to the removal of pharmaceutical and other pollutants of emerging concern, Curr. Opin. Green Sustain. Chem. 29 (2021), 100458, https://doi.org/10.1016/j.cogsc.2021.100458.

[20] W. Li, X. Geng, F. Xiao, G. An, D. Wang, FeII/FeIII Doped Bi/BiOBr hierarchical microspheres as a highly efficient catalyst for degradation of organic contaminants at neutral pH: the role of visible light and H2O2, ChemCatChem 9 (2017) 3762–3771, https://doi.org/10.1002/cctc.201700549.

[21] J. Li, J. You, Z. Wang, Y. Zhao, J. Xu, X. Li, H. Zhang, Application of α-Fe2O3-based heterogeneous photo-Fenton catalyst in wastewater treatment: a review of recent advances, J. Environ. Chem. Eng. 10 (5) (2022), 108329, https://doi.org/10.1016/j.jece.2022.108329.

[22] F. Velichkova, C. Julcour-Lebigue, B. Koumanova, H. Delmas, Heterogeneous Fenton oxidation of paracetamol using iron oxide (nano)particles, J. Environ. Chem. Eng. 1 (2013) 1214–1222, https://doi.org/10.1016/j.jece.2013.09.011.

[23] C.B. Molina, E. Sanz-Santos, A. Boukhemkhem, J. Bedia, C. Belver, J. Rodriguez, Removal of emerging pollutants in aqueous phase by heterogeneous Fenton and photo-Fenton with Fe2O3-TiO2-clay heterostructures, Environ. Sci. Pollut. Res. 27 (2020) 38434–38445, https://doi.org/10.1007/s11356-020-09236-8.

[24] M. Kohantorabi, G. Moussavi, P. Oulego, S. Giannakis, Deriving an α-Fe2O3/g-C3N4 nanocomposite from a naturally hematite-rich soil, for dual photocatalytic and photo-Fenton degradation of Acetaminophen under visible light, Sep. Purif. Technol. 299 (2022), 121723, https://doi.org/10.1016/j.seppur.2022.121723.

[25] J. Li, C. Li, N. de Oliveira, L.A.C. dos Santos, L.C.C. Teixeira, Removal of diethyltoluamide, paracetamol, caffeine and triclosan from natural water by photo-Fenton process using powdered zero-valent iron, J. Water Process Eng. 48 (2022), 102907, https://doi.org/10.1016/j.jwpe.2022.102907.

[26] B. Palanivel, C. Hu, M. Shkir, S. AlFaify, F.A. Ibrahim, M.S. Hamdy, A. Mani, Fluorine doped g-C3N4 coupled NiFe2O4 heterojunction: Consumption of H2O2 for production of hydroxyl radicals towards paracetamol degradation, Colloids Interface Sci. Commun. 42 (2021), 100410, https://doi.org/10.1016/j.colcom.2021.100410.

[27] S.S. Imam, R. Adnan, N.H. Mohd Kaus, The photocatalytic potential of BiOBr for wastewater treatment: a mini-review, J. Environ. Chem. Eng. 9 (4) (2021), 105404, https://doi.org/10.1016/j.jece.2021.105404.

[28] L. Meng, Y. Qu, L. Jing, Recent advances in BiOBr-based photocatalysts for environmental remediation, Chinese Chem. Lett. 32 (2021) 3265–3276, https://doi.org/10.1016/j.cclet.2021.03.083.

[29] M.Y.N. Núñez, M.Á. Rehlaender, A. Martínez-de la Cruz, A. Susarrey-Arce, F. M. Cuevas-Muñiz, M. Sánchez-Domínguez, T.E. Lara-Ceniceros, J. Bonilla-Cruz, A. A. Zapata, P.C. Hurtado, M. Pérez-Rodríguez, A.R. Orozco, L.T. González, F. E. Longoria-Rodríguez, Enhancing visible light photocatalytic degradation of bisphenol A Using BiOI/Bi2MoO6 heterostructures, Nanomaterials 13 (2023) 1503, https://doi.org/10.3390/NANO13091503.

[30] K. López-Velázquez, J.L. Guzmán-Mar, A. Hernández-Ramírez, E. González-Juárez, M. Villanueva-Rodríguez, Synthesis of Fe–BiOBr–N by microwave-assisted solvothermal method: characterization and evaluation of its photocatalytic properties, Mater. Sci. Semicond. Process. 123 (2021), 105499, https://doi.org/10.1016/j.mssp.2020.105499.

[31] W. An, H. Wang, T. Yang, J. Xu, Y. Wang, D. Liu, J. Hu, W. Cui, Y. Liang, Enriched photocatalysis-Fenton synergistic degradation of organic pollutants and coking wastewater via surface oxygen vacancies over Fe-BiOBr composites, Chem. Eng. J. 451 (2022), 138653, https://doi.org/10.1016/j.cej.2022.138653.

[32] Z. Liu, B. Wu, Y. Zhu, D. Yin, L. Wang, Fe-Ions Modified BiOBr mesoporous microspheres with excellent photocatalytic property, Catal. Letters. 142 (2012) 1489–1497, https://doi.org/10.1007/s10562-012-0899-9.

[33] M. Yuan, F. Tian, G. Li, H. Zhao, Y. Liu, R. Chen, Fe(III)-Modified BiOBr hierarchitectures for improved photocatalytic benzyl alcohol oxidation and organic pollutants degradation, Ind. Eng. Chem. Res. 56 (2017) 5935–5943, https://doi.org/10.1021/acs.iecr.7b00905.

[34] M.T.H. Siddiqui, F.L. Chan, S. Nizamuddin, H.A. Baloch, S. Kundu, M. Czajka, G. J. Griffin, A. Tanksale, K. Shah, M. Srinivasan, Comparative study of microwave and conventional solvothermal synthesis for magnetic carbon nanocomposites and bio-oil from rice husk, J. Environ. Chem. Eng. 7 (4) (2019), 103266, https://doi.org/10.1016/J.JECE.2019.103266.

[35] B. Dhokale, A. Susarrey-Arce, A. Pekkari, A. Runemark, K. Moth-Poulsen, C. Langhammer, H. Härelind, M. Busch, M. Vandichel, H. Sundén, Microwave-heated γ-alumina applied to the reduction of aldehydes to alcohols, ChemCatChem 12 (2020) 6344–6355, https://doi.org/10.1002/cctc.202001284.

[36] Y.-L. Cai, Y.-H. Xu, J.-Z. Xiang, Z.-Q. Zhang, Q.-X. He, Y.-F. Li, J. Lü, Iron–doped bismuth oxybromides as visible–light–responsive Fenton catalysts for the degradation of tetrazine in aqueous phases, J. Environ. Sci. (2023), https://doi.org/10.1016/j.jes.2023.01.005.

[37] N.A. Khan, V. Vambol, S. Vambol, B. Bolibrukh, M. Sillanpaa, F. Changani, A. Esrafili, M. Yousefi, Hospital effluent guidelines and legislation scenario around the globe: a critical review, J. Environ. Chem. Eng. 9 (5) (2021), 105874, https://doi.org/10.1016/j.jece.2021.105874.

[38] N.O.M. Nom–semarnat-, D. Norma, O. Mexicana, O. Mexicana, Dof: 11/03/2022, (2022) 11–12.

[39] Z. Chen, J. Zeng, J. Di, D. Zhao, M. Ji, J. Xia, H. Li, Facile microwave-assisted ionic liquid synthesis of sphere-like BiOBr hollow and porous nanostructures with enhanced photocatalytic performance, Green Energy Environ. 2 (2) (2017) 124–133.

[40] A. Han, H. Zhang, D. Lu, J. Sun, G.K. Chuah, S. Jaenicke, Efficient photodegradation of chlorophenols by BiOBr/NaBiO3 heterojunctioned composites under visible light, J. Hazard. Mater. 341 (2018) 83–92, https://doi.org/10.1016/j.jhazmat.2017.07.031.

[41] L. Cao, D. Ma, Z. Zhou, C. Xu, C. Cao, P. Zhao, Q. Huang, Efficient photocatalytic degradation of herbicide glyphosate in water by magnetically separable and recyclable BiOBr/Fe3O4 nanocomposites under visible light irradiation, Chem. Eng. J. 368 (2019) 212–222, https://doi.org/10.1016/j.cej.2019.02.100.

[42] C. Guo, Y. He, P. Du, X. Zhao, J. Lv, W. Meng, Y. Zhang, J. Xu, Novel magnetically recoverable BiOBr/iron oxides heterojunction with enhanced visible light-driven photocatalytic activity, Appl. Surf. Sci. 320 (2014) 383–390, https://doi.org/10.1016/j.apsusc.2014.09.111.

[43] S. Bhatt, A. Malik, A. Soni, B. Moses Abraham, A. Sen, S.L. Jain, Photocatalytic reductive carboxylation of terminal alkynes with CO2using heterostructured ZIF-7/

[44] BiOBr under visible-light illumination, J. CO2 Util. 67 (2023), 102334, https://doi.org/10.1016/j.jcou.2022.102334.

[44] S.K. Arumugasamy, S. Govindaraju, K. Yun, Manganese ions conjugated on layered bismuth oxyhalides for high-performance pseudocapacitors and efficient oxygen evolution catalysts, Inorg. Chem. Front. 7 (2020) 4412–4423, https://doi.org/10.1039/d0qi00776e.

[45] X. Geng, W. Li, F. Xiao, D. Wang, L. Yang, Effect of: In situ Fe(II)/Fe(IIi)-doping on the visible light-Fenton-like catalytic activity of Bi/BiOBr hierarchical microspheres, Catal Sci. Technol. 7 (2017) 658–667, https://doi.org/10.1039/c6cy02195f.

[46] P.-Q. Wang, J.-Y. Liu, Y.-Q. Hu, Y. Bai, Z. Fan, N, C-codoped BiOCl flower-like hierarchical structures, Micro Nano Lett. 7 (2012) 876–879, https://doi.org/10.1049/mnl.2012.0496.

[47] G. Jiang, X. Wang, Z. Wei, X. Li, X. Xi, R. Hu, B. Tang, R. Wang, S. Wang, T. Wang, W. Chen, Photocatalytic properties of hierarchical structures based on Fe-doped BiOBr hollow microspheres, J. Mater. Chem. A 1 (2013) 2406–2410, https://doi.org/10.1039/c2ta00942k.

[48] J. Wang, Y. Zhang, L. Tian, F. Liu, Q. Xia, Ultrathin BiOBr nanocrystals with dominant 001 facets and their high photocatalytic activity, J. Nanoparticle Res. 16 (2014) 2691, https://doi.org/10.1007/s11051-014-2691-9.

[49] X.J. Wang, Y. Zhao, F.T. Li, L.J. Dou, Y.P. Li, J. Zhao, Y.J. Hao, A Chelation strategy for in-situ constructing surface oxygen vacancy on 001 facets exposed BiOBr nanosheets, Sci. Rep. 6 (2016) 24918, https://doi.org/10.1038/srep24918.

[50] D. Wu, S. Yue, W. Wang, T. An, G. Li, H.Y. Yip, H. Zhao, P.K. Wong, Boron doped BiOBr nanosheets with enhanced photocatalytic inactivation of Escherichia coli, Appl. Catal. B Environ. 192 (2016) 35–45, https://doi.org/10.1016/j.apcatb.2016.03.046.

[51] Y. Yan, H. Yang, Z. Yi, X. Wang, R. Li, T. Xian, Evolution of Bi Nanowires from BiOBr Nanoplates through a NaBH4 reduction method with enhanced photodegradation performance, Environ. Eng. Sci. 37 (2020) 64–77, https://doi.org/10.1089/ees.2019.0284.

[52] W. An, H. Wang, T. Yang, J. Xu, Y. Wang, D. Liu, J. Hu, wenquan Cui, Y. Liang, Surface Oxygen Vacancies and Photocatalysis-Fenton Synergistic Enhance the Degradation of Organic Pollutants and Coking Wastewater by Fe-Biobr Composites, SSRN Electron. J. https://doi.org/10.2139/ssrn.4119152.

[53] X. Chen, X. Zhang, Y.H. Li, M.Y. Qi, J.Y. Li, Z.R. Tang, Z. Zhou, Y.J. Xu, Transition metal doping BiOBr nanosheets with oxygen vacancy and exposed 102 facets for visible light nitrogen fixation, Appl. Catal. B Environ. 281 (2021) 119516, https://doi.org/10.1016/j.apcatb.2020.119516.

[54] A. Liu, J. Liu, B. Pan, W.X. Zhang, Formation of lepidocrocite (γ-FeOOH) from oxidation of nanoscale zero-valent iron (nZVI) in oxygenated water, RSC Adv. 4 (2014) 57377–57382, https://doi.org/10.1039/c4ra08988j.

[55] N. Thomas, D.D. Dionysiou, S.C. Pillai, Heterogeneous Fenton catalysts: a review of recent advances, J. Hazard. Mater. 404 (2021), 124082, https://doi.org/10.1016/j.jhazmat.2020.124082.

[56] J. He, X. Yang, B. Men, D. Wang, Interfacial mechanisms of heterogeneous Fenton reactions catalyzed by iron-based materials: a review, J. Environ. Sci. (China) 39 (2016) 97–109, https://doi.org/10.1016/j.jes.2015.12.003.

[57] K.C. Devarayapalli, P.V. K, S.V. Prabhakar Vattikuti, J. Shim, 3D flower-like BiOBr prepared via solvothermal method for methanol oxidation and supercapacitor application, Chem. Pap. 76 (1) (2022) 259–265.

[58] Y. Liu, J. Li, J. Li, X. Yan, F. Wang, W. Yang, D.H.L. Ng, J. Yang, Active magnetic Fe3+-doped BiOBr micromotors as efficient solar photo-fenton catalyst, J. Clean. Prod. 252 (2020), 119573, https://doi.org/10.1016/j.jclepro.2019.119573.

[59] Z. Cai, J. Zhong, J. Li, H. Jin, Oxygen vacancies enriched BiOBr with boosted photocatalytic behaviors, Inorg. Chem. Commun. 126 (2021), 108450, https://doi.org/10.1016/j.inoche.2021.108450.

[60] M.M. Hinojosa Guerra, I. Oller Alberola, S. Malato Rodriguez, A. Agüera López, A. Acevedo Merino, A. Egea-Corbacho Lopera, J.M. Quiroga Alonso, Oxidation mechanisms of amoxicillin and paracetamol in the photo-Fenton solar process, Water Res. 156 (2019) 232–240, https://doi.org/10.1016/j.watres.2019.02.055.

[61] A.M. Huerta-Flores, F. Ruiz-Zepeda, C. Eyovge, J.P. Winczewski, M. Vandichel, M. Gaberšček, N.D. Boscher, H.J.G.E. Gardeniers, L.M. Torres-Martínez, A. Susarrey-Arce, Enhanced Photocatalytic Hydrogen Evolution from Water Splitting on Ta2O5/SrZrO3Heterostructures Decorated with CuxO/RuO2Cocatalysts, ACS Appl. Mater. Interfaces 14 (2022) 31767–31781, https://doi.org/10.1021/acsami.2c02520.

[62] S.A. Lozano-Morales, G. Morales, M.Á. López Zavala, A. Arce-Sarria, F. Machuca-Martínez, Photocatalytic treatment of paracetamol using TiO2 nanotubes: effect of pH, Processes. 7 (2019) 1–9, https://doi.org/10.3390/pr7060319.

[63] H. Idriss, On the wrong assignment of the XPS O1s signal at 531–532 eV attributed to oxygen vacancies in photo- and electro-catalysts for water splitting and other materials applications, Surf. Sci. 712 (2021), 121894, https://doi.org/10.1016/j.susc.2021.121894.